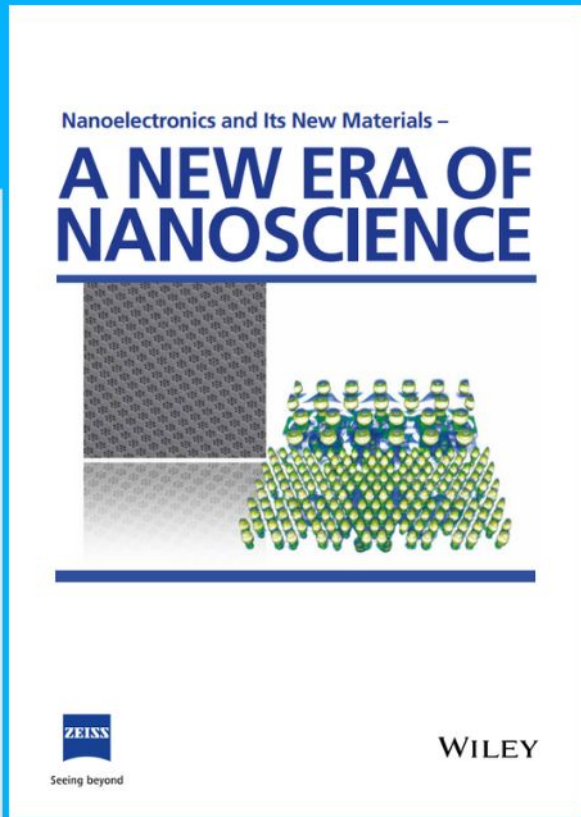




# Nanoelectronics and Its New Materials – A NEW ERA OF NANOSCIENCE



**Discover the recent advances in electronics research and fundamental nanoscience.**

Nanotechnology has become the driving force behind breakthroughs in engineering, materials science, physics, chemistry, and biological sciences. In this compendium, we delve into a wide range of novel applications that highlight recent advances in electronics research and fundamental nanoscience. From surface analysis and defect detection to tailored optical functionality and transparent nanowire electrodes, this eBook covers key topics that will revolutionize the future of electronics.

To get your hands on this valuable resource and unleash the power of nanotechnology, simply download the eBook now. Stay ahead of the curve and embrace the future of electronics with nanoscience as your guide.



Seeing beyond

**WILEY**

# High Anti-Jamming Flexible Capacitive Pressure Sensors Based on Core–Shell Structured AgNWs@TiO<sub>2</sub>

Renhou Han, Yue Liu, Yepi Mo, Huichen Xu, Zhengwen Yang,\* Rongrong Bao,\* and Caofeng Pan\*

Flexible capacitive pressure sensors play an important role in electronic skin and human–machine interaction due to their high sensitivity and convenient preparation, comparing with those resistive/piezoresistive sensors. However, due to the complexity of the application environment, reported capacitive sensors often experience signal instability by electromagnetic interference and proximity effects. The great challenge for capacitive sensors is to maintain sensitivity and wide linear range while reducing interference. This study proposes a high anti-jamming capacitive flexible pressure sensor with polyvinylidene fluoride (PVDF)@AgNWs@TiO<sub>2</sub> film as the dielectric layer. Core–shell structure-based AgNWs@TiO<sub>2</sub> is embedded into the PVDF film. The introduction of the core–shell structure not only enhances the initial capacitance but also balances the dielectric constant, dielectric loss, and breakdown strength of the dielectric layer. The sensor is validated to exhibit a high signal-to-noise ratio for a variety of interference sources and is demonstrated with an intelligent glove sensing system, which provides a new idea for developing a high anti-jamming capacitive flexible pressure sensor.

## 1. Introduction

Flexible pressure sensors as the next generation of electronic devices play a vital role in electronic skin,<sup>[1–7]</sup> man–machine interaction,<sup>[8–11]</sup> medical security monitoring,<sup>[12–16]</sup> and soft robotics.<sup>[17–19]</sup> Flexible capacitive sensors occupy a place under unique advantages, such as high precision, low power consumption, and low dependence on external conditions.<sup>[20–24]</sup> However, limited by physical dimension, their capacitance is usually low, resulting in a higher output impedance, which makes capacitive sensors prone to instability due to electromagnetic jamming and proximity effects.<sup>[25–27]</sup> There are few solutions to the anti-jamming problem of capacitance sensors at present. Therefore, electromagnetic shielding measures, generally consisting of metallic meshes or screens, must be taken, which brings inconvenience to the design and use of capacitive sensors.<sup>[28,29]</sup>

On the other hand, the parasitic capacitance will be increased between the shield and sensing electrodes due to shielding measures. Compared with the constant parasitic capacitance of traditional rigid devices, it will be changed with the deformation of flexible devices due to the corresponding change in the distance between the shield and the sensing electrode under pressure.<sup>[30,31]</sup> Therefore, for flexible devices,<sup>[32]</sup> it is difficult to be compensated for the readout and obtain stable and high signal-to-noise ratio (SNR) operation.<sup>[33]</sup> As a result, implementation of the flexible capacitive devices with anti-jamming (A-J), high sensitivity, softness, and strong mechanical robustness is a challenge to be tackled.

In this context, dielectric materials exhibiting a high dielectric constant and low dielectric loss have been developed as optimal strategies to address the underlying issue.<sup>[34,35]</sup> These materials elicit a pronounced electric field cancellation effect, wherein an external electric field induces an opposing electric field. Moreover, the magnitude of this additional electric field amplifies with higher applied electric field intensities, thereby promoting a more uniform electric field distribution. The attainment of a high dielectric constant in polymer films is accomplished by incorporating a small concentration of metal particles within the polymer matrix.<sup>[36–39]</sup> Consequently, dielectric layers possessing elevated dielectric constants substantially augment both the initial capacitance ( $C_0$ ) and the relative capacitance change ( $\Delta C$ ), while

R. Han, H. Xu, C. Pan  
Center on Nanoenergy Research  
School of Physical Science and Technology  
Guangxi University  
Nanning, Guangxi 530004, P. R. China  
E-mail: cfpan@binn.cas.cn

R. Han, Y. Liu, Y. Mo, H. Xu, R. Bao, C. Pan  
CAS Center for Excellence in Nanoscience  
Beijing Key Laboratory of Micro-nano Energy and Sensor  
Beijing Institute of Nanoenergy and Nanosystems  
Chinese Academy of Sciences  
Beijing 101400, P. R. China  
E-mail: baorongrong@binn.cas.cn

Y. Liu, Y. Mo, R. Bao, C. Pan  
School of Nanoscience and Engineering  
University of Chinese Academy of Sciences  
Beijing 100049, P. R. China

Y. Liu, Z. Yang  
College of Materials Science and Engineering  
Kunming University of Science and Technology  
Kunming 650093, P. R. China  
E-mail: yangzw@kust.edu.cn

 The ORCID identification number(s) for the author(s) of this article can be found under <https://doi.org/10.1002/adfm.202305531>

DOI: 10.1002/adfm.202305531

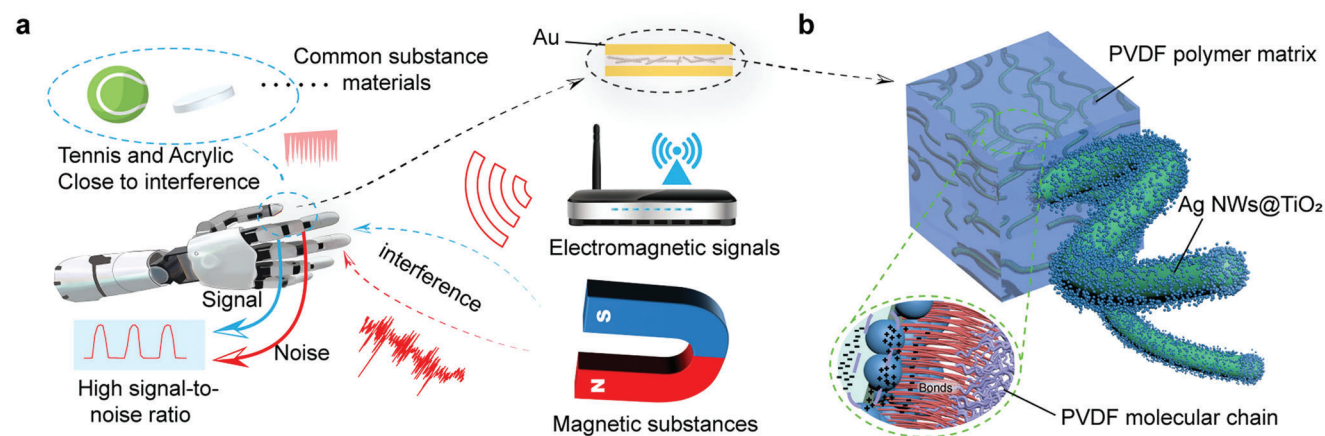


**Figure 1.** High SNR capacitive sensor based on core-shell structure. a) Electromagnetic signals, magnetic field changes, and common objects near jamming to maintain a high SNR. b) Schematic diagram of the microstructure of the medium layer and intermolecular interactions.

concurrently ensuring a constant parasitic capacitance. As a result, the sensor's signal-to-noise ratio is effectively enhanced.

However, the majority of organic polymers used in flexible devices show low dielectric constant. Although some of these have relatively high dielectric constants, their dielectric losses are usually high, especially at high electric fields. Metals as good conductors ensure the metal-filled polymer composites with a typical percolation system, that is, the dielectric constant of the composite will be increased with the increase of the loading amount of metal nanoparticles before the percolation threshold.<sup>[40–42]</sup> Thus, the composite of multiphase materials provides a greater possibility for adjusting and optimizing the properties of dielectric materials for flexible capacitive sensors.<sup>[43–45]</sup> However, metal doping of the insulation layer tends to cause partial discharges, which results in electric field distortion at the interface and reduces the breakdown strength of the device. Meanwhile, when the mismatch between the conductivity of the polymer matrix and the introduced filler is large, the formation of interfacial bonds is usually a key factor in obtaining the desired dielectric properties in composites, which affects the uniform dispersion of nanoparticles and the polymer/nanoparticle interfacial properties.<sup>[46]</sup> Therefore, the realization of a proper balance between dielectric constant,<sup>[47]</sup> dielectric loss,<sup>[48]</sup> and breakdown strength for high-performance composites and the application of the composites in flexible A-J capacitive devices still faces many challenges.

Herein, an A-J flexible capacitive pressure sensor based on three-phase composites has been developed for an intelligent glove-sensing system. Firstly, polyvinylidene fluoride (PVDF) as a flexible matrix exhibits a high dielectric constant due to its obvious ferroelectric characteristics, the strong polarity of the C–F bond within the molecular chain, and the spontaneous alignment of the dipole. Secondly, a certain amount of silver nanowires (Ag-NWs) has been introduced into the PVDF matrix, and the dielectric constant is further improved by the percolation effect of the conductive particles in the insulating polymer matrix. Thirdly, to attenuate the interfacial electrical mismatch between PVDF and AgNWs and the electrical percolation transition in composite, a core-shell structure has been constructed by grafting TiO<sub>2</sub> as a buffer layer on the surface of AgNWs. As a result, both the ini-

tial capacitance and dielectric constant of PVDF@AgNWs@TiO<sub>2</sub> films are  $\approx 1.5$  times compared to pure PVDF films. Moreover, a proper balance is achieved between dielectric constant, dielectric loss, and breakdown strength, which is essential for the preparation of nanocomposites with high overall performance. On this basis, an A-J capacitive pressure sensor is integrated using the PVDF@AgNWs@TiO<sub>2</sub> film as a dielectric layer, whose A-J capability has been verified by excitation in various simulated natural environments and compared with common flexible polymer materials used for dielectric layers. Additionally, the device demonstrates a high sensitivity of  $0.0012 \text{ kPa}^{-1}$  over an ultra-wide sensing range of within 1500 kPa and super-stable loading-unloading cycles over 33 000 times in noisy environments. Finally, by integrating with the back-end circuit system and intelligent glove sensing system that can transmit wirelessly via Bluetooth are developed, which provides a new idea for the development of flexible A-J capacitive pressure sensors.

## 2. Results and Discussion

### 2.1. Design Concept of a High A-J Capacitive Pressure Sensor

Achieving high A-J of flexible capacitive pressure sensors with a high SNR in different environmental fields is desired, as shown in Figure 1a, which requires improving the dielectric constant of the device while balancing it with the relationship between dielectric loss and breakdown strength. The fabrication process of the devices can be found in Figure S1 (Supporting Information). However, flexible sensors are usually based on polymers, which generally show a low dielectric constant. The doping of metal fillers with high dielectric constants plays a key role in improving the dielectric constant of materials. However, metal doping of the insulation layer tends to cause partial discharges that produce electrical dendrites and the electric field distortion at the interface both can cause a reduction in the breakdown strength of the device. Improved interfaces allow for more uniform dispersion of metal particles and hinder the formation of electrical channels. Therefore, the improvement of the interface between the polymer and the metal filler is crucial.

The introduction of TiO<sub>2</sub> nanoparticles on the high aspect ratio metal surface is the most hopeful way to solve the problem. TiO<sub>2</sub> has a high density of oxygen vacancies and generally exhibits the characteristics of an n-type semiconductor. Since the Fermi levels of TiO<sub>2</sub> and AgNWs are different (Figure S2, Supporting Information), more electrons are transferred from TiO<sub>2</sub> to AgNWs, and the surface of TiO<sub>2</sub> shows positive charges while the surface of AgNWs shows negative charges. Meanwhile, the polar interaction between the electronegative fluorine in the –CF<sub>3</sub> of PVDF and the positive charge in TiO<sub>2</sub> creates a negatively charged region at the PVDF–TiO<sub>2</sub> interface as shown in the larger view of Figure 1b.<sup>[46]</sup> The strong bonding between TiO<sub>2</sub> and PVDF (red in illustration) causes core–shell structured metal NWs to disperse evenly in the polymer and prevents the formation of electrical channels. This explains that the introduction of TiO<sub>2</sub> improves the dielectric loss and breakdown strength in PVDF@AgNWs. Matrix material PVDF with high dielectric constant and fillers AgNWs@TiO<sub>2</sub> with unique core–shell structure are compounded as the dielectric layer.<sup>[49–51]</sup> Then, it is integrated with the upper and lower gold electrodes into a sandwich structure for the preparation of A-J capacitive pressure sensors in Figure 1a.

## 2.2. Characterization of Core–Shell Structured AgNWs@TiO<sub>2</sub>

The doping of AgNWs@TiO<sub>2</sub> has been found to have negligible impact on the properties of the PVDF film. The resulting composite films retain excellent characteristics in terms of softness, transmissivity, and thinness, as demonstrated in Figure 2a. Further details and specific data can be found in the supporting information, specifically in Figures S3, S4, and S9 (Supporting Information). To demonstrate the successful preparation of composite films, the wide-angle X-ray diffraction (XRD) patterns of PVDF@AgNWs@TiO<sub>2</sub> core–shell nanoparticles and pure PVDF are shown in Figure 2b. Two substances are observed at about  $2\theta = 20.2^\circ$  for the  $\beta$  (110/200) phase of PVDF. Consistent with the reported results.<sup>[52]</sup> The  $2\theta$  values at  $38.2^\circ$ ,  $44.4^\circ$ ,  $64.4^\circ$ , and  $77.2^\circ$  corresponds to the (110), (200), (220), (331) crystal planes of Ag<sup>0</sup> in the core–shell structure nanoparticles, respectively.<sup>[53]</sup> Here, the TiO<sub>2</sub> is amorphous, so the TiO<sub>2</sub> phase cannot be checked. Scanning electron microscope (SEM) images in Figure S5a (Supporting Information) and Figure 2c reveal that the surface of AgNWs becomes rough upon the introduction of TiO<sub>2</sub>, indicating the formation of a uniform core–shell structure. Additionally, Figure S5 (Supporting Information) demonstrates that the morphology of the silver lines did not undergo significant changes before and after the ultrasound treatment. In addition, energy dispersive spectroscopy (EDS) mapping of PVDF@AgNWs@TiO<sub>2</sub> films shows the distribution of each element of Ag, O, and Ti, demonstrating that TiO<sub>2</sub> nanoparticles are uniformly distributed on the AgNWs skeleton (Figure 2c). The transmission electron microscopy (TEM) images illustrate this more clearly in Figure 2d-i. Crystal characteristics of TiO<sub>2</sub> show lattice fringes with a lattice spacing of 3.67 Å at the crystal plane (110) for Figure 2d-ii.

The surface composition of the AgNWs@TiO<sub>2</sub> is characterized by the X-ray photoelectron spectroscopy (XPS) technique. At a binding energy of 284.8 eV, C 1s reaches its peak.<sup>[54]</sup> The XPS

survey spectrum of the nanocomposite confirms the presence of O 1s, Ag 3d, Ti 2s, and Ti 2p for Figure 2e-i. Figure 2e-ii–iv shows the XPS spectra of O 1s, Ti 2p, and Ag 3d, respectively. Figure 2e-ii displays the XPS spectrum of O 1s, which displays an asymmetric peak, implying the presence of several oxygen species. The oxygen species has a high binding energy (O 1sC, 532.5 eV). The deconvolution peaks of O 1s located at 530.2 and 531.9 eV correspond to O 1sA and O 1sB, respectively.<sup>[55]</sup> Figure 2e-iii shows two peaks (458.5 and 464.3 eV) respectively, were seen in the Ti 2p nuclear level spectrum, suggesting Ti 2p<sub>3/2</sub> and Ti 2p<sub>1/2</sub> states. The 5.7 eV gap between these peaks and their positions implies that Ti<sup>4+</sup> is formed in TiO<sub>2</sub>.<sup>[56]</sup> In the high-resolution XPS spectrum of Ag 3d, Ag 3d peaks are divided into two peaks, namely Ag 3d 5/2 (367.5 eV) and 3d 3/2 (373.2 eV). Ag (3d 5/2) has two deconvolution peaks at 367.5 and 368.4 eV, and Ag (3d 3/2) has two deconvolution peaks at 373.2 and 374.3 eV. The peaks of 367.5 and 373.2 eV (5.7 eV bimodal distance) correspond to the Ag<sup>0</sup> component of the metal,<sup>[57]</sup> while the peaks of 368.4 and 374.3 eV correspond to Ag<sup>+</sup>.<sup>[58,59]</sup>

## 2.3. Dielectric Properties of PVDF@AgNWs@TiO<sub>2</sub> Composite Films

The dielectric properties of PVDF@AgNWs@TiO<sub>2</sub> film have been characterized and compared with pure PVDF and PVDF@AgNWs. A schematic diagram of the composite film is shown in Figure 3a and the illustrations show the SEM images of AgNWs@TiO<sub>2</sub> and a cross-sectional view of the composited film.

Initial capacitance with the same area of three films at different frequencies is shown in Figure 3b. Due to the influence of the dielectric constant, the initial capacitance of PVDF@AgNWs film, PVDF@AgNWs@TiO<sub>2</sub> film, and PVDF film shows a decreasing trend in sequence. The initial capacitance of PVDF@AgNWs film is 12.1 pF, PVDF@AgNWs@TiO<sub>2</sub> film is 10.70 pF and PVDF film is 8.71 pF (80 kHz). A large initial capacitance value is positive for improving the SNR of the device.

The dielectric constant is obtained from the calculation the formula is that:

$$\epsilon = \frac{4k\pi dC}{S} \quad (1)$$

where  $\epsilon$  is the dielectric constant of the dielectric layer,  $k$  is the electrostatic force constant,  $S$  is the area directly opposite the capacitance pole plate,  $d$  is the distance between the two pole plates, and  $C$  is the capacitance.

The test results of the dielectric constant of the three films have been shown in Figure 3c. Commonly, the pure PVDF film demonstrates the lowest value of 5.11 (80 kHz). We also calculated that the dielectric constants of PDMS and Ecoflex are 1.24 and 2.1, respectively, which are much smaller than those of PVDF, and this is the reason why we chose PVDF. The low percolation threshold of metallic materials means that the composite material can have a high dielectric constant with a small amount of filler. Under a suitable filler filling in this experiment, the dielectric constant of PVDF/AgNWs films is calculated to be about 7.0 (80 kHz). As for PVDF@AgNWs@TiO<sub>2</sub> film, TiO<sub>2</sub> nanoparticles as the interface buffer layer between

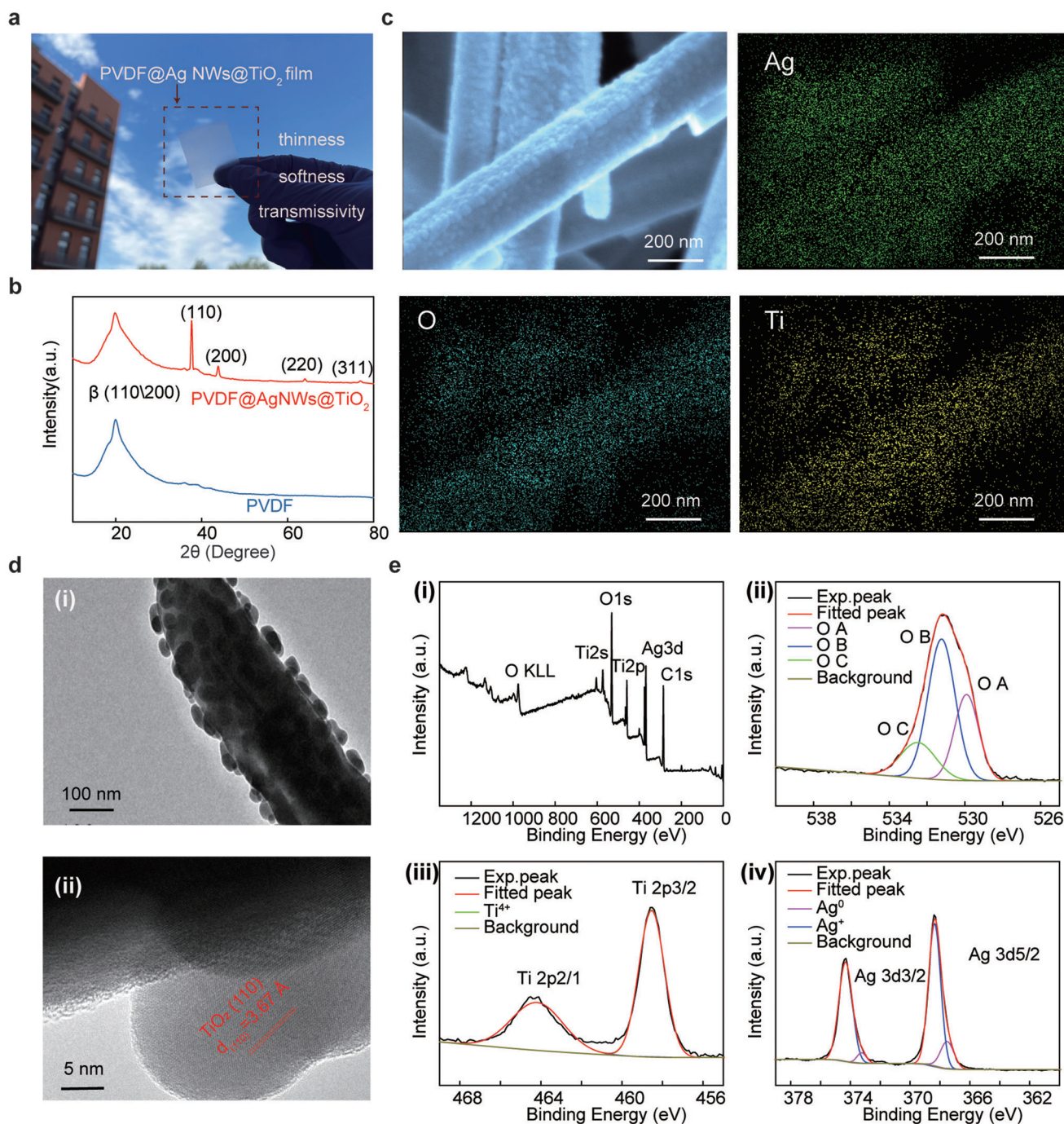


**Figure 2.** Basic characterization of core-shell structure. a) PVDF@AgNWs@TiO<sub>2</sub> film optical image. b) Pure PVDF and PVDF@AgNWs@TiO<sub>2</sub> XRD patterns. c) EDS mapping image of Ag, O, and Ti elements corresponding to AgNWs@TiO<sub>2</sub> core-shell nanocomposites (scale 200 nm). d) TEM image of the core-shell structure and titanium dioxide particles. e) XPS spectra of AgNWs@TiO<sub>2</sub> core-shell, i) XPS measurement spectra, ii) high-resolution XPS spectra of O 1s, iii) high-resolution XPS spectra of Ti 2p, iv) high-resolution XPS spectra of Ag 3d.

the initial filler and the polymer enhance the interface polarization and limit the movement and transmission of electrons between conductive particles. Compared with the PVDF@AgNWs film, TiO<sub>2</sub> doping increased the percolation threshold, resulting in a slight decrease in the dielectric constant. The dielectric constant of PVDF@AgNWs@TiO<sub>2</sub> film is calculated to be about 6.3 (80 kHz) in this experiment.

The dielectric loss is obtained from the calculation the formula is:

$$\epsilon^* = \epsilon' - i\epsilon'', \quad \tan\delta = \frac{\epsilon''}{\epsilon'} \quad (2)$$

where  $\epsilon^*$  is complex permittivity, which consists of real ( $\epsilon'$ ) and imaginary ( $\epsilon''$ ) parts,  $\tan\delta$  is Dielectric loss. As can be seen from

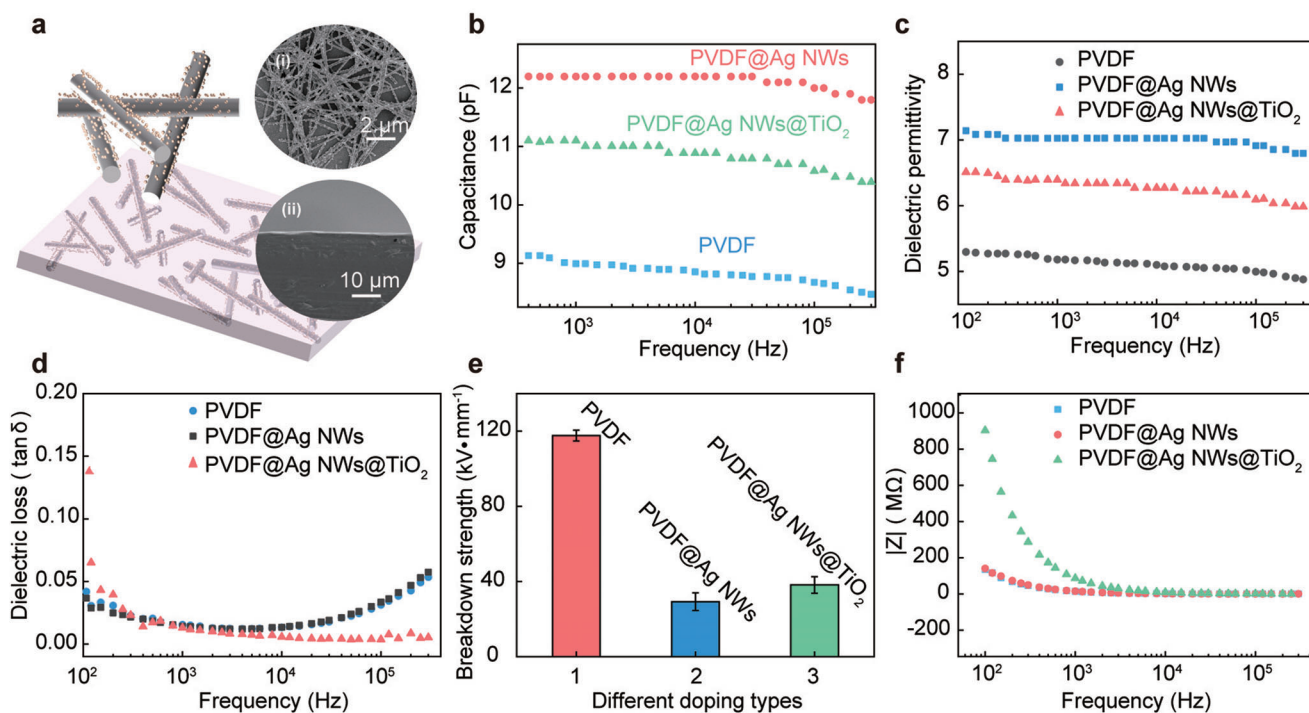


**Figure 3.** Basic electrical properties of PVDF@AgNWs@TiO<sub>2</sub> composite films. a-i) SEM image of the modification Ag nanowires, ii) SEM image of the cross-section of the modification Ag nanowires. b) The relationship between the initial capacitance and frequency of PVDF, PVDF@AgNWs, and PVDF@AgNWs@TiO<sub>2</sub> nanocomposite films. c) Relationship between dielectric constant and frequency of PVDF, PVDF@AgNWs, and PVDF@AgNWs@TiO<sub>2</sub> nanocomposite films. d) Relationship between dielectric loss and frequency of PVDF, PVDF@AgNWs, and PVDF@AgNWs@TiO<sub>2</sub> nanocomposite films. e) Breakdown strength of PVDF, PVDF@AgNWs, and PVDF@AgNWs@TiO<sub>2</sub>. f) Relation between impedance and frequency of PVDF, PVDF@AgNWs, and PVDF@AgNWs@TiO<sub>2</sub> nanocomposite films.

Figure 3d,  $\tan \delta$  fluctuates at a low frequency of  $10^2$ – $10^3$  Hz. Loss occurs at high frequencies (80 kHz), and the dielectric loss of pure PVDF is up to 0.027. The PVDF@AgNWs film has a large leakage current due to the addition of AgNWs, which increases the seepage effect. Thus, the dielectric loss is up to 0.03 at a high frequency (80 kHz). The introduction of the insulating layer of TiO<sub>2</sub> restricts the transfer of electrons of AgNWs, which plays a blocking role internally. So the dielectric loss of PVDF@AgNWs@TiO<sub>2</sub> film at high frequency (80 kHz) is only 0.0039.

The electrical breakdown strength of the three films is shown in Figure 3e. Pure PVDF film is a single-phase material with high purity, so the breakdown voltage reaches  $117.68 \text{ kV mm}^{-1}$ . While PVDF@AgNWs films due to the presence of AgNWs, the mixing of heterogeneous materials produces poor compatibility and an inhomogeneous electric field, leading to the generation of leakage current, resulting in a breakdown strength of  $29.32 \text{ kV mm}^{-1}$ . With the introduction of TiO<sub>2</sub>, an effective reduction in leakage current is achieved with a breakdown strength of  $38.33 \text{ kV mm}^{-1}$ , but it is still difficult to get rid of the inhomogeneous electric field generated by the mixing of multiphase materials.

The frequency-impedance curves of the three films are shown in Figure 3f. At low frequencies of  $10^2$ – $10^3$  Hz, the introduction of the insulating layer TiO<sub>2</sub> effectively hinders the potential formation of a conductive network of AgNWs in the interfacial region, exhibiting a high impedance. This phenomenon also shows the superiority of the core-shell structure. At  $10^3$ – $10^5$  Hz, the impedance of the composite material decreases gradually with

increasing frequency, most likely due to the excitation of charge carriers inside the material at high frequencies. At this point, the impedance of all samples is about  $3.17 \text{ M}\Omega$ , indicating that the composite material has good insulation, which is conducive to their practical application.

We also examined the influence of different TiO<sub>2</sub> contents on the dielectric parameters of the films, as depicted in Figure S6 (Supporting Information) of the supporting information. The base capacitance and dielectric constant values of all three compositions were found to be relatively similar. With an increase in the TiO<sub>2</sub> content, the proportion of AgNWs in the total solution decreases, while both components possess high dielectric constants. Consequently, the base capacitance and dielectric constants of the tested films exhibit a comparable trend after blending with PVDF polymer. However, the higher TiO<sub>2</sub> content inhibits the formation of a silver nanowire network, impeding electron movement and reducing the percolation effect. The formation of a titanium dioxide shell layer subsequently leads to reduced dielectric loss and enhanced impedance in the film.

#### 2.4. Electrical Performances of the Capacitance Pressure Sensor

The parameter optimization experiments are shown in Figure 4a, where the sensing performances of the devices with AgNWs@TiO<sub>2</sub> doping are demonstrated. Since Young's modulus of the fillers (AgNWs@TiO<sub>2</sub>) is large relative to that of the PVDF matrix material, as the dielectric properties of the

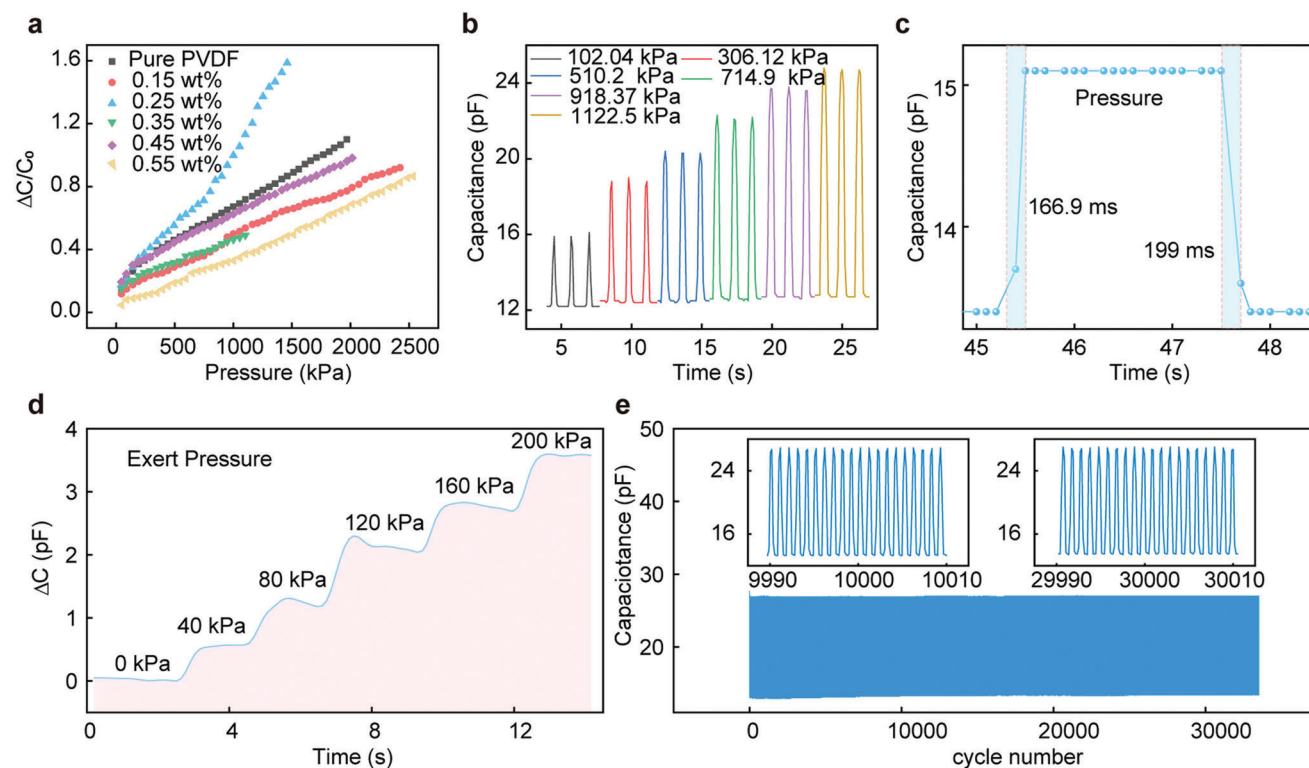


**Figure 4.** The basic sensing performance of capacitance sensor. a) Effects of different doping PVDF@AgNWs@TiO<sub>2</sub> content on sensing performance. b) Dynamic responses of the sensor to different external pressure cycles. c) Response time and recovery time. d) The step test response of the sensor to different pressure stable. e) Stability of 33 000 loading/unloading cycles at 1122.5 kPa.

composite change, so does it is Young's modulus, which in turn affects the ability of the device to deform when subjected to compression. Therefore, the dielectric properties of the composite are considered to have a harmonious relationship with Young's modulus, and an optimal value of filler doping should exist at this point. The highest sensitivity is obtained when the doping content is 0.25 wt%, showing 0.0012 kPa<sup>-1</sup> with a fitted linearity of 0.98 over a wide range of 1500 kPa. Figure 4b shows the stable and fast dynamic response of the device at different pressures. More pressure response signals are shown in Figure S7 (Supporting Information). Response times and recovery times of the device are 166.9 and 199 ms, respectively (Figure 4c). To test the stability of the continuous load, the stepped response under different pressures is tested, and a relatively stable response is generated under different gradients, as shown in Figure 4d. As can be seen in Figure 4e, the fluctuations are very small during 33 000 loading/unloading cycles at a high pressure of 1122.5 kPa, proving that the device has good cycling stability. Figure S8 (Supporting Information) demonstrates that the fitted curves of the actual and applied pressure values of the force tester are in general agreement.

## 2.5. A-J Performances of the Capacitance Pressure Sensor

The PVDF@AgNWs@TiO<sub>2</sub>-based capacitive sensors were placed in a variety of environments to subject them to electromagnetic interference and proximity interference to verify their

superior immunity to interference. The common different kinds of materials (acrylic, fabric, metal, human body) and the interference of cell phone electromagnetic waves on the capacitive signal of the device are shown in Figure 5a. The capacitance decreases slightly when the interference source is close to the device, but the value of this change is largely negligible compared to the strength of the pressure response. An enlarged plot of the capacitive response when the interference source is closed is shown in Figure 5b, with small signal fluctuations.

In Figure 5c we compare the signal-to-noise ratio of pure PVDF and PVDF@AgNWs@TiO<sub>2</sub>. The signal-to-noise ratio of the PVDF@AgNWs@TiO<sub>2</sub> structure is also all-around higher than that of pure PVDF in the presence of different interference sources. To further demonstrate the immunity of film to interference demonstrate its excellent immunity to interference, the PVDF@AgNWs@TiO<sub>2</sub> films are compared with common flexible dielectric materials. To mitigate the influence of thickness on capacitance, we maintained a consistent film thickness of ≈24 μm for all three materials. This approach significantly minimizes the capacitance error arising from variations in thickness. The thickness cross-sections can be found in Figure S9 (Supporting Information) of the supporting information. The variation of the non-contact capacitance of the three dielectric materials in the proximity of the five interference sources is demonstrated in Figure 5d. It can be seen that the variation value of PVDF@AgNWs@TiO<sub>2</sub> film is around 0.1 pF when the interference source is close, and this value is slightly lower than Ecoflex and PDMS. However, the response values and detectable

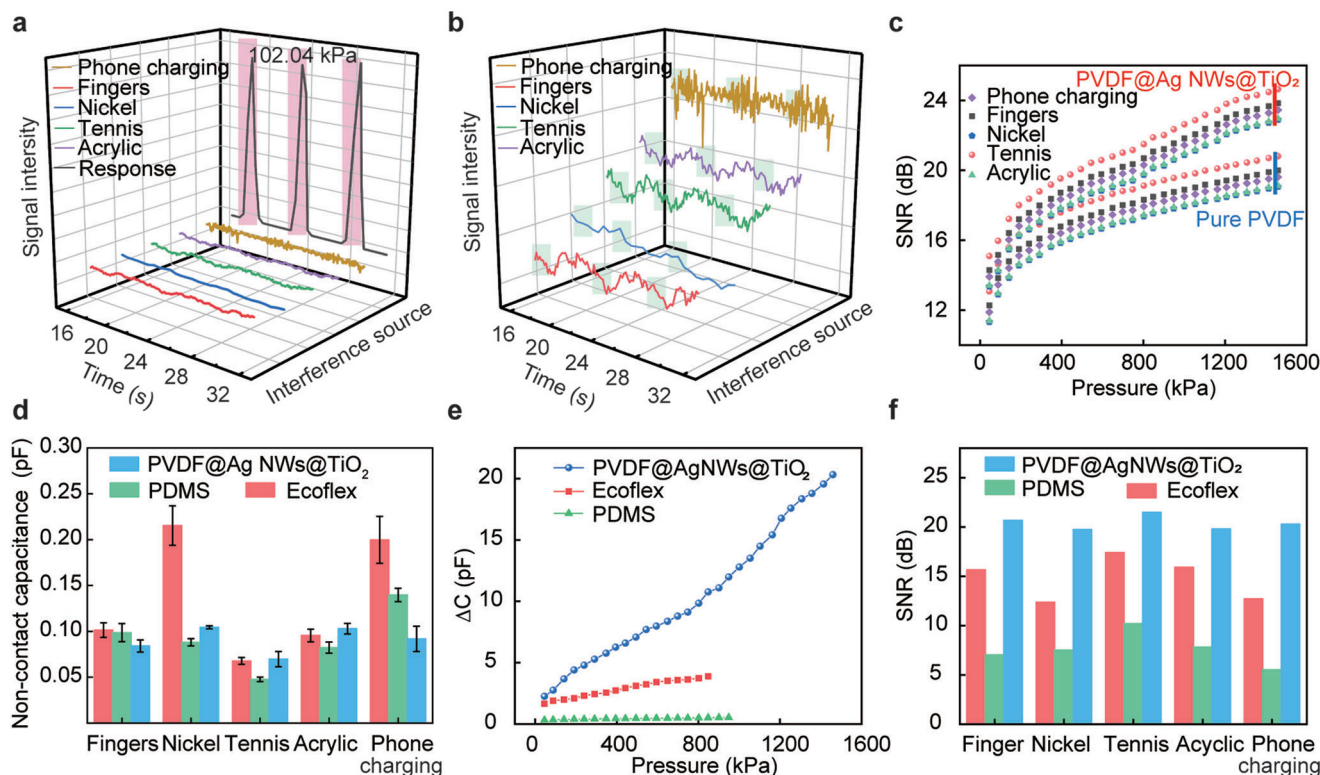


**Figure 5.** The A-J performance test of the sensor. a) The comparison between the pressure signal and the five signal intensities. b) Describes the intensity of the five jamming signals. c) Comparison of signal-to-noise ratio between PVDF@AgNWs@TiO<sub>2</sub> and pure PVDF. d) The change of the relative capacitance of three different materials under the non-contact jamming in five different situations. e) Capacitance change of three different materials under pressure. f) The size of the SNR of different materials under different jamming sources.

range of PVDF@AgNWs@TiO<sub>2</sub> film to effective pressure are much higher than those of Ecoflex film and PDMS film in Figure 5e. This may be due to the higher initial dielectric constant resulting in higher detection sensitivity. In addition, due to the increase in the electrical breakdown strength of the material, the thinning of the dielectric layer can increase the capacitance and weaken the edge effect, further improving the sensitivity and detectable range of the device. The SNR is defined as the ratio of the capacitive response signal of the effective pressure to the capacitive fluctuation signal of the proximity of the interference source. Figure 5f shows the SNR of the three dielectric materials at 802.04 kPa, where the PVDF@AgNWs@TiO<sub>2</sub> film exhibits higher values under various environmental disturbances, proving its better immunity to interference (The data plot at multiple pressures is shown in Figure S10, Supporting Information).

## 2.6. Integration of A-J Glove Sensing Systems

The A-J gloves mainly consist of a 5-channel capacitive pressure sensor array, a data acquisition (DAQ) circuit with a wireless transmitter, and a personal computer (PC) terminal with a wireless receiver in Figure 6a. PVDF@AgNWs@TiO<sub>2</sub> film (i, ii) and PDMS film (iii, iv) are selected as the dielectric layers, respectively, to realize the device preparation and integration in the glove sensing system. The optical photos are shown in Figure 6b.

The gloves with a dielectric layer of PDMS are used as a non-interference-resistant (N-I-R) device, which is used as a comparison with the A-J device. Figure 6c shows the corresponding signal changes when the N-I-R device grabs the cup with and without water, proving that the water will have a great impact on the capacitance signal value, indicating that this device cannot achieve the purpose of A-J. However, in Figure 6d, when the device is an A-J device, the capacitance changes of the glove gripping the cup with and without water are almost the same, which proves that the A-J device is more scientific, credible and stable than ordinary devices in practical applications. Additionally, experiments with the continuous and fast grasping of objects with the A-J glove sensing system are validated, here with a balloon. When gripping continuously, the capacitive response signal appears as a distinct plateau Figure 6e, when continuously squeezing the balloon, the signal appears as a distinct peak Figure 6f. Visibly, the A-J glove sensing system has an obvious response to grasping objects and obvious recognition for continuous and continuously squeezing. Moreover, grabbing the ear wash ball and the single-finger pulse test are also validated (Figures S11 and S12, Supporting Information).

## 3. Conclusions

A high A-J capacitive flexible pressure sensor with PVDF@AgNWs@TiO<sub>2</sub> film as the dielectric layer has been proposed. PVDF is used as the matrix material for the dielectric

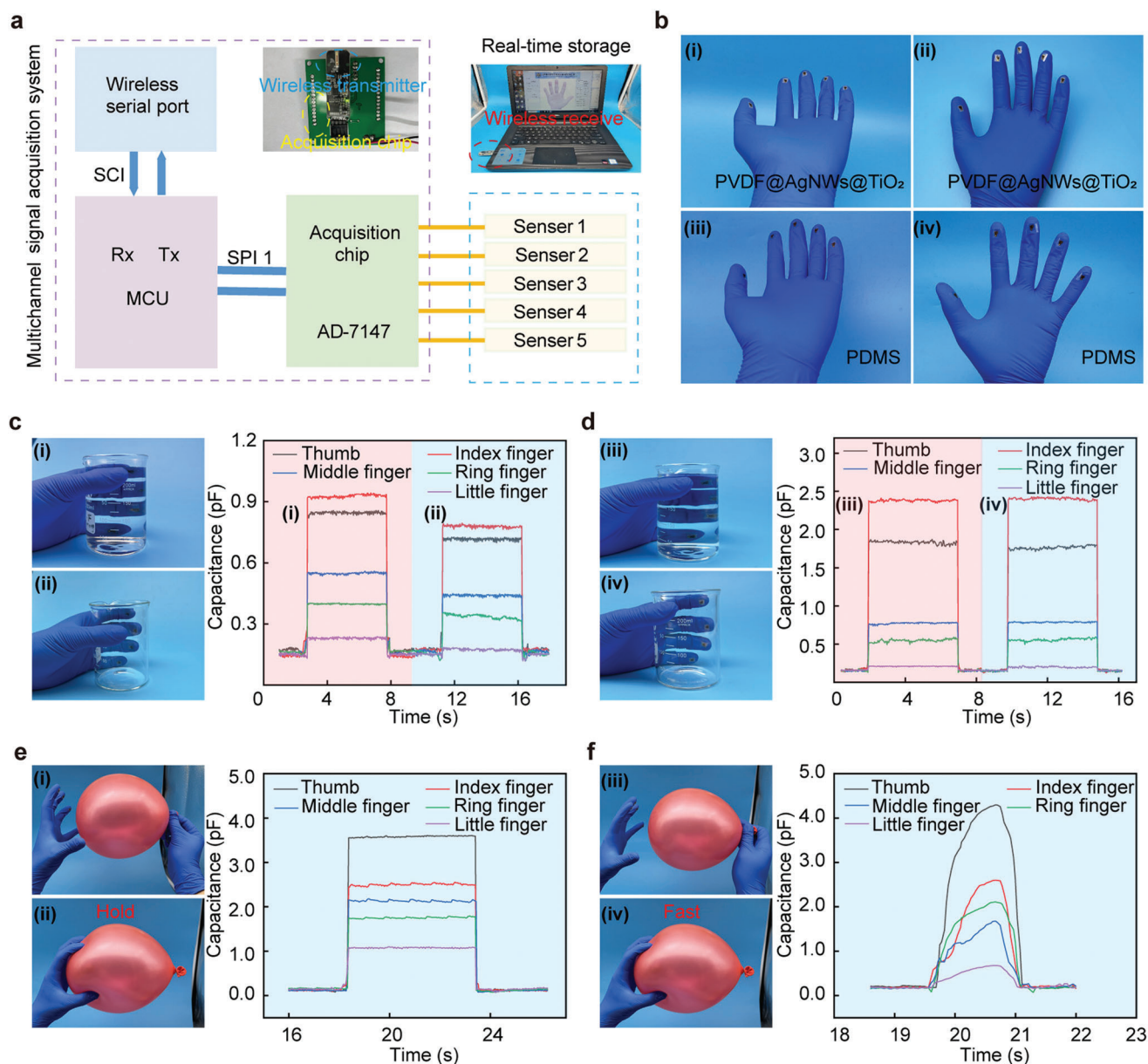


**Figure 6.** The A-J test of tactile gloves. a) Tactile glove principle circuit diagram, five channels capacitive pressure sensor tactile glove, DAQ circuit module with a wireless transmitter, PC terminal with wireless receiver three parts. b-i,ii) The PVDF@AgNWs@TiO<sub>2</sub> dielectric layer sensor, and iii,iv) The PDMS dielectric layer sensor. c) PDMS dielectric layer tactile glove holds water and anhydrous beakers figure capacitance variation chart. d) PVDF@AgNWs@TiO<sub>2</sub> dielectric layer tactile glove holds water and anhydrous beaker figure capacitance variation chart. e,f) The capacitance signal change value of holding and continuously squeezing the balloon, respectively.

layer, whose dielectric constant is higher than that of commonly used flexible materials. The AgNWs@TiO<sub>2</sub> based on core-shell structure as the fillers of the dielectric layer achieves an effective balance of dielectric constant, dielectric loss and breakdown strength of the composite materials. In addition, the sensing performance of the devices prepared by the composite materials is improved due to the combined enhancement of their dielectric properties. Tests with different interference sources close to the device are also implemented, and the capacitance signal shows small fluctuations, which are largely negligible compared to the

capacitance response signal at effective pressure. Compared with common flexible dielectric materials, such as Ecoflex and PDMS, the composite material shows even more significant advantages. Its SNR is above 20 dB under different disturbances. Finally, the device is integrated into the gloves and combined with the back-end circuit system to design an A-J glove sensing system. In the practical application, the gloves demonstrate excellent A-J capability and provide a reliable and scientific way to solve the problem of the poor A-J capability of flexible capacitive pressure sensors.

## 4. Experimental Section

**Materials:** AgNWs/DMF dispersion solution purchased from Nano Chemical Guangzhou, ethylene glycol (EG, 99.9%), titanium (IV) butoxide (TBT, 97%), were purchased from Sinopharm Group (P. R. China). *N,N*-Dimethylformamide (DMF, C<sub>3</sub>H<sub>7</sub>NO, MW = 73.09), Aladdin Reagents (Shanghai) Co., LTD. PVDF powder (HSF 900, MW = 950 000) was purchased from Dongguan Huachuang Plasticization Co. LTD. Flexible electrode sheet from Shenzhen Kailutong Technology Co. The device mainly composed of is a sandwich structure of a flexible electrode sheet, a dielectric layer, and a flexible electrode sheet, using copper wires to lead the electrodes.

**Synthesis of PVDF@AgNWs@TiO<sub>2</sub> Films:** First, 0.1 mL TBT solution was added to 10 mL EG solution with a pipette gun and stirred at room temperature for 8 h with a magnetic stirring apparatus to obtain TBT/EG (titanium dioxide precursor) mixed solution. Next, DMF solution 5 mL (5 mg mL<sup>-1</sup>) and TBT/EG 0.1 mL titanium dioxide precursor solution of AgNWs were ultrasonic for 60 min to produce a core-shell structure AgNWs@TiO<sub>2</sub>. Then 0.75 g PVDF powder was weighed, 10 mL DMF and 1 mL AgNWs@TiO<sub>2</sub> solution were taken, and the three solutions were mixed and stirred with magnetic apparatus at 60 °C and 1000 rpm for 4 h. Finally, apply 1.5 mL PVDF@AgNWs@TiO<sub>2</sub> mixed solution to the mold (2.5 × 7.5), wipe well, and let stand for 30 min to make the surface of the solution more uniform, and put the sample in the oven at 70 °C for 8 h to dry into a film. Finally, remove with tweezers.

**Preparation of Pure PVDF Films for Electrical Properties Test:** The pure PVDF film was prepared by weighing 0.75 g PVDF powder mixed with 11 mL DMF solution and stirring at 60 °C and 1000 rpm for 4 h. After coating 1.5 mL solution in the mold (2.5 × 7.5), the solution was evenly spread and left for 30 min to make the surface of the solution more uniform. The sample was dried in the oven at 70 °C for 8 h to form a pure PVDF film.

**PVDF@AgNWs@TiO<sub>2</sub> Breakdown Strength Test for Thin Film Preparation:** Take 8 mL PVDF@AgNWs@TiO<sub>2</sub> mixed solution to the mold (10 × 10), wipe well, and let stand for 30 min to make the surface of the solution more uniform, and put the sample in the oven at 70 °C for 8 h to dry into a film. Then remove with tweezers. The pure PVDF films for the breakdown strength test were prepared as described above.

**Measurements and Characterizations:** The XRD (xpret3 powder) diffraction angles of 10–90° (40 kV/40 Ma) in the 2θ Angle range were studied for the crystal phases of the composites. Nova Nano SEM 450 (Czech Republic) scanning electron microscope images and EDS spectroscopy to detect the uniform distribution of elements. F20 TEM (Transmission Electron Microscope) took a high-resolution transmission electron microscope image. The load sensor (HZC-T-10KG), linear motor (R-LP3), and LCR meter (E980-AL-30) were used to test all capacitance signals and dielectric parameters of the device. A heating magnetic agitator (MS7-H550-PRO), oven (DKN312C), ultrasonic cleaning machine (KQ-800KDE), and balance (Mettler PL-402) were used for sample preparation. The breakdown strength of the films was tested with a breakdown voltmeter (DDJ-50 kV).

The data acquisition and information processing chip were designed with the implementation of a multi-channel capacitance signal acquisition module (AD7147) to capture analog signals obtained from the tactile skin sensors. These analog signals were then converted into a digital format and transmitted to the micro control unit (MCU) through the utilization of the serial peripheral interface communication protocol. The MCU module (PIC16F1526) played a vital role in programming the data acquisition, processing, and control functionalities of the tactile sensor. Furthermore, the acquired sensing information was subsequently transmitted to the computer by means of the asynchronous serial port. To facilitate this transmission, the transistor-transistor logic digital signals were converted to the standard RS-232 level with the assistance of a MAX3232 driver chip.

## Supporting Information

Supporting Information is available from the Wiley Online Library or from the author.

## Acknowledgements

R.H.H. and Y.L. contributed equally to this work. The authors thank the support of Natural Science Foundation of Beijing Municipality (2222088 and Z180011), National key R&D program of China (2021YFB3200302 and 2021YFB3200304), National Natural Science Foundation of China (Nos. 52125205, U20A20166, and 52192614), Shenzhen Science and Technology Program (Grant No. KQTD20170810105439418), and the Fundamental Research Funds for the Central Universities.

## Conflict of Interest

The authors declare no conflict of interest.

## Data Availability Statement

The data that support the findings of this study are available from the corresponding author upon reasonable request.

## Keywords

capacitive pressure sensors, core-shell structure, dielectric constant, high signal-to-noise ratio

Received: May 18, 2023

Revised: July 11, 2023

Published online:

- [1] J. Li, Z. Yuan, X. Han, C. Wang, Z. Huo, Q. Lu, M. Xiong, X. Ma, W. Gao, C. Pan, *Small Sci.* **2022**, *2*, 2100083.
- [2] Y. Liu, J. Tao, W. K. Yang, Y. F. Zhang, J. Li, H. L. Xie, R. R. Bao, W. C. Gao, C. F. Pan, *Small* **2022**, *18*, 2106906.
- [3] J. Tao, M. Dong, L. Li, C. F. Wang, J. Li, Y. Liu, R. R. Bao, C. F. Pan, *Microsyst. Nanoeng.* **2020**, *6*, 62.
- [4] Y. X. Wan, J. Tao, M. Dong, L. Zhang, Z. C. Peng, R. R. Bao, C. F. Pan, *Adv. Mater. Technol.* **2022**, *7*, 2200386.
- [5] G. Ge, W. Yuan, W. Zhao, Y. Lu, Y. Z. Zhang, W. J. Wang, P. Chen, W. Huang, W. L. Si, X. C. Dong, *J. Mater. Chem.* **2019**, *7*, 5949.
- [6] G. Ge, Y. Lu, X. Y. Qu, W. Zhao, Y. F. Ren, W. J. Wang, Q. Wang, W. Huang, X. C. Dong, *ACS Nano* **2020**, *14*, 218.
- [7] Y. Lu, X. Y. Qu, W. Zhao, Y. F. Ren, W. L. Si, W. J. Wang, Q. Wang, W. Huang, X. C. Dong, *Research* **2020**, *2020*, 2038560.
- [8] B. C. K. Tee, C. Wang, R. Allen, Z. N. Bao, *Nat. Nanotechnol.* **2012**, *7*, 825.
- [9] Y. Liu, H. Y. Xu, M. Dong, R. H. Han, J. Tao, R. R. Bao, C. F. Pan, *Adv. Mater. Technol.* **2022**, *7*, 2200504.
- [10] R. Bao, J. Tao, C. Pan, Z. L. Wang, *Small Sci.* **2021**, *1*, 2000060.
- [11] K. Zheng, F. Gu, H. J. Wei, L. J. Zhang, X. Chen, H. L. Jin, S. Pan, Y. H. Chen, S. Wang, *Small Methods* **2023**, *7*, 2201534.
- [12] W. Gao, S. Emaminejad, H. Y. Y. Nyein, S. Challa, K. V. Chen, A. Peck, H. M. Fahad, H. Ota, H. Shiraki, D. Kiriya, D. H. Lien, G. A. Brooks, R. W. Davis, A. Javey, *Nature* **2016**, *529*, 509.
- [13] C. Hou, G. Tai, Y. Liu, Z. Wu, X. Liang, X. Liu, *Nano Res. Energy* **2023**, *2*, e9120051.
- [14] J. Ren, W. Zhang, Y. Wang, Y. Wang, J. Zhou, L. Dai, M. Xu, *InfoMat* **2019**, *1*, 396.
- [15] R. Garg, N. Driscoll, S. Shankar, T. Hullfish, E. Anselmino, F. Iberite, S. Averbek, M. Rana, S. Micera, J. R. Baxter, F. Vitale, *Small Methods* **2023**, *7*, 2201318.
- [16] Y. Khan, A. E. Ostfeld, C. M. Lochner, A. Pierre, A. C. Arias, *Adv. Mater.* **2016**, *28*, 4373.

- [17] C. M. Boutry, M. Negre, M. Jorda, O. Vardoulis, A. Chortos, O. Khatib, Z. N. Bao, *Sci. Robot.* **2018**, *3*, 6914.
- [18] Y. Wang, Z. H. Zhang, H. X. Chen, H. Zhang, H. Zhang, Y. J. Zhao, *Sci. Bull.* **2022**, *67*, 512.
- [19] J. N. Ma, Y. L. Zhang, Y. Q. Liu, D. D. Han, J. W. Mao, J. R. Zhang, W. C. Zhao, H. B. Sun, *Sci. Bull.* **2022**, *67*, 501.
- [20] Y. Liu, R. R. Bao, J. Tao, J. Li, M. Dong, F. C. Pan, *Sci. Bull.* **2020**, *65*, 70.
- [21] R. B. Mishra, N. El-Atab, A. M. Hussain, M. M. Hussain, *Adv. Mater. Technol.* **2021**, *6*, 2001023.
- [22] J. Qin, L. J. Yin, Y. N. Hao, S. L. Zhong, D. L. Zhang, K. Bi, Y. X. Zhang, Y. Zhao, Z. M. Dang, *Adv. Mater.* **2021**, *33*, 2008267.
- [23] K. H. Ha, W. Zhang, H. Jang, S. Kang, L. Wang, P. Tan, H. Hwang, N. Lu, *Adv. Mater.* **2021**, *33*, 2103320.
- [24] T. Cheng, X. L. Yang, S. Yang, L. Li, Z. T. Liu, J. Qu, C. F. Meng, X. C. Li, Y. Z. Zhang, W. Y. Lai, *Adv. Funct. Mater.* **2023**, *33*, 2210997.
- [25] S. R. A. Ruth, V. R. Feig, M. G. Kim, Y. Khan, J. K. Phong, Z. N. Bao, *Small Struct.* **2021**, *2*, 2000079.
- [26] D. Yoo, D. J. Won, W. Cho, J. Lim, J. Kim, *Adv. Mater. Technol.* **2021**, *6*, 2100358.
- [27] T. Schlegl, H. Zangl, presented at 17th Conference on Sensors and Their Applications, Dubrovnik, Croatia, Sep 16–18, **2013**.
- [28] H. B. Wang, J. Kow, N. Raske, G. de Boer, M. Ghajari, R. Hewson, A. Alazmani, P. Culmer, *Sens. Actuators, A* **2018**, *271*, 44.
- [29] B. Aksoy, Y. F. Hao, G. Grasso, K. M. Digumarti, V. Caccuciolo, H. Shea, *Nat. Commun.* **2022**, *13*, 4649.
- [30] P. Roberts, D. D. Damian, W. L. Shan, T. Lu, C. Majidi, IEEE International Conference on Robotics and Automation (ICRA). Soft-matter capacitive sensor for measuring shear and pressure deformation. Karlsruhe, Germany, May 06–10, **2013**.
- [31] H. B. Wang, M. Totaro, L. Beccai, IEEE 26th IEEE International Conference on Electronics, Circuits and Systems (ICECS), Genoa, Italy, Nov 27–29, **2019**.
- [32] K. Wang, W. Xu, W. Zhang, X. Wang, X. Yang, J. Li, H. Zhang, J. Li, Z. Wang, *Nano Res. Energy* **2023**, *2*, e9120042.
- [33] C. M. Boutry, L. Beker, Y. Kaizawa, C. Vassos, H. Tran, A. C. Hinckley, R. Pfattner, M. Niu, J. H. Li, J. Claverie, Z. Wang, J. Chang, P. M. Fox, Z. N. Bao, *Nat. Biomed. Eng.* **2019**, *3*, 47.
- [34] X. Y. Huang, P. K. Jiang, *Adv. Mater.* **2015**, *27*, 546.
- [35] S. K. Hwang, I. Bae, S. M. Cho, R. H. Kim, H. J. Jung, C. Park, *Adv. Funct. Mater.* **2013**, *23*, 5484.
- [36] Y. Bai, L. Sun, Q. Yu, Y. Lei, B. Liu, *Nano Res. Energy* **2023**, *2*, e9120043.
- [37] L. Meng, L. Li, *Nano Res. Energy* **2022**, *1*, e9120020.
- [38] J. D. Musah, A. M. Ilyas, S. Venkatesh, S. Mensah, S. Kwofie, V. A. L. Roy, C.-M. L. Wu, *Nano Res. Energy* **2022**, *1*, e9120034.
- [39] Y. Xu, H. Xue, X. Li, X. Fan, P. Li, T. Zhang, K. Chang, T. Wang, J. He, *Nano Res. Energy* **2023**, *2*, e9120052.
- [40] W. Zheng, X. F. Lu, W. Wang, Z. J. Wang, M. X. Song, Y. Wang, C. Wang, *Phys. Status Solidi A* **2010**, *207*, 1870.
- [41] M. Panda, V. Srinivas, A. K. Thakur, *Appl. Phys. Lett.* **2008**, *92*, 132905.
- [42] X. Y. Huang, P. K. Jiang, L. Y. Xie, *Appl. Phys. Lett.* **2009**, *95*, 242901.
- [43] Z. B. Pan, L. M. Yao, J. W. Zhai, B. Shen, S. H. Liu, H. T. Wang, J. H. Liu, *J. Mater. Chem. A* **2016**, *4*, 13259.
- [44] X. Zhang, Y. Shen, Q. Zhang, L. Gu, Y. Hu, J. Du, Y. Lin, C. W. Nan, *Adv. Mater.* **2015**, *27*, 819.
- [45] G. Jian, C. Zhang, C. Yan, K. S. Moon, C. P. Wong, *ACS Appl. Nano Mater.* **2018**, *1*, 1396.
- [46] M. Rahimabady, M. S. Mirshekarloo, K. Yao, L. Lu, *Phys. Chem.* **2013**, *15*, 16242.
- [47] G. Li, S. H. Yu, R. Sun, presented at 15th International Conference on Electronic Packaging Technology (ICEPT), Chinese Institute of Electronics, Chengdu, Peoples Republic China, Aug 12–15, **2014**.
- [48] H. Zhu, Z. Liu, F. H. Wang, K. Yan, *RSC Adv.* **2016**, *6*, 64634.
- [49] J. J. Qiu, T. T. Yang, Y. F. Li, W. H. Qian, X. Y. Liu, *Rare Met.* **2022**, *41*, 630.
- [50] J. C. Ma, U. Azhar, C. Y. Zong, Y. B. Zhang, A. H. Xu, C. C. Zhai, L. Q. Zhang, S. X. Zhang, *Mater. Des.* **2019**, *164*, 107556.
- [51] K. Yu, Y. J. Niu, Y. C. Zhou, Y. Y. Bai, H. Wang, *J. Am. Ceram. Soc.* **2013**, *96*, 2519.
- [52] H. Y. Xu, J. Tao, Y. Liu, Y. P. Mo, R. R. Bao, C. F. Pan, *Small* **2022**, *18*, 2202477.
- [53] X. H. Yang, H. T. Fu, L. T. Zhang, X. Z. An, S. X. Xiong, X. C. Jiang, A. B. Yu, *Sens. Actuators, B* **2019**, *286*, 483.
- [54] H. H. Yin, K. Yu, C. Q. Song, R. Huang, Z. Q. Zhu, *ACS Appl. Mater. Interfaces* **2014**, *6*, 14851.
- [55] Y. V. Kaneti, J. Moriceau, M. Liu, Y. Yuan, Q. M. Zakaria, X. Jiang, A. Yu, *Sens. Actuators, B* **2015**, *209*, 889.
- [56] Y. Yu, W. Wen, X. Y. Qian, J. B. Liu, J. M. Wu, *Sci. Rep.* **2017**, *7*, 41253.
- [57] H. Zhang, D. Wang, C. H. Sheng, D. P. Ben, H. L. Wu, N. T. Mao, *Fibers Polym.* **2021**, *22*, 597.
- [58] G. B. Hoflund, Z. F. Hazos, G. N. Salaita, *Phys. Rev. B* **2000**, *62*, 11126.
- [59] X. H. Yang, H. T. Fu, K. Wong, X. C. Jiang, A. B. Yu, *Nanotechnology* **2013**, *24*, 415601.